Supporting Information

Material and Methods

Protein preparation and labeling. A pET47b(+)-based plasmid for the expression of the protein L FRET mutant (C7-C64) with an N-terminal His6-tag and a subsequent recognition site for HRV 3C protease was obtained from Celtek Genes (Franklin, USA). Two more protein L variants, the protein L PET mutant (C64) and control mutant (F47-C64) were generated using site-directed mutagenesis. All three variants were expressed recombinantly in E. coli BL21(DE3). 2 L cultures were grown in LB medium to $OD_{600} \approx 0.8$ and then induced with 1 mM IPTG for 4 hours at 37°C. After harvesting by centrifugation, the cells were resuspended in Lysis Buffer (100 mM NaH_2PO_4 and 10 mM Tris, 6 M GdmCl, 10 mM imidazole, pH 8). His_6-tagged protein L was purified from the soluble fraction of the lysate using Ni Sepharose (GE Healthcare Bio-Sciences AB, Uppsala, Sweden). Bound protein was eluted with a gradient of 10 to 170 mM imidazole in Lysis Buffer. The pooled fractions containing protein L were subjected to one-step refolding and cleavage of the His6-tag. Refolding of protein L was achieved by dialysis against Cleavage Buffer (100 mM NaH_2PO_4, 100 mM NaCl, 1 mM DTT, pH 7.4) after adding HRV 3C Protease (produced in-house) at a protein-to-protease molar ratio of about 100 to 1. The cleavage reaction was stopped by adding GdmCl to a final concentration of 4.8 M. The His_6-tag containing peptide and uncleaved protein were separated from protein L using a 5 ml HisTrap column (GE Healthcare Bio-Sciences AB, Uppsala, Sweden). Protein L in the flow-through fractions was reduced with 50 mM DTT, concentrated and subjected to gel filtration using a Superdex 75 10/300 GL column (GE Healthcare Bio-Sciences AB, Uppsala, Sweden) in 100 mM NaH_2PO_4, 6 M GdmCl, pH 7.1. The protein L FRET variant was labeled with Alexa Fluor 488 maleimide (Molecular Probes, Eugene, USA) at a dye/protein molar ratio of 0.7/1 for 2 h at room temperature, and subsequently with Alexa Fluor 594 maleimide at a dye/protein molar ratio of 2/1 over night at 4 °C. The protein L PET variants were labeled with ATTO-Oxa11 maleimide (ATTO-TEC GmbH, Siegen, Germany) at a dye/protein molar ratio of 3/1 for 3 h at room temperature. Unreacted dyes were removed by gel filtration using a Superdex 75 10/300 GL column (GE Healthcare Bio-Sciences AB, Uppsala, Sweden) in 100 mM NaH_2PO_4, 6 M GdmCl, pH 7.1. The correct molecular mass of all labeled protein samples was verified by electrospray ionization mass spectrometry.

Single-molecule fluorescence spectroscopy. Single-molecule fluorescence measurements were performed with a MicroTime 200 confocal microscope (PicoQuant, Germany) equipped with an Olympus UplanApo 60x/1.20W objective (Olympus). For single-molecule FRET measurements, a diode laser (LDH-D-C-485, PicoQuant, Germany) was synchronized with a 20 MHz supercontinuum laser (SC-450-4, Fianium, UK) filtered by a z582/15 band pass filter (Chroma) for pulsed interleaved excitation (PIE) (66) of labeled molecules. For FRET-FCS measurements, the same diode laser was used in continuous-wave mode to excite the donor dye. Photons emitted from the sample were collected by the objective, and scattered light was suppressed by a filter (HQ500LP, Chroma Technology) before the emitted photons passed the confocal pinhole (100 μm diameter). The emitted photons were then distributed into four channels, first by a polarizing beam splitter and then by a dichroic mirror (585DCXR, Chroma) for each polarization. Donor and acceptor emission was filtered (ET525/50m or HQ650/100m, respectively, Chroma Technology) and then focused on a τ-SPAD avalanche photodiode (PicoQuant). The arrival time of every detected photon was recorded with a HydraHarp 400 counting module (PicoQuant). For PET-FCS measurements, a Helium Neon laser at 632.8 nm (05-LHP-925, Melles Griot) was employed to excite ATTO-Oxa11. The collected photons were separated into two channels by a polarizing beam splitter (zt 633 RDC, Chroma), filtered with

a band pass filter (ET685/50, Chroma) and an IR-filter (HC 720/SP, Semrock), and detected by τ-SPAD avalanche photodiodes (PicoQuant). All experiments were performed on molecules freely diffusing in solution.

FRET experiments were performed by exciting the donor dye with a laser power of 100 μW (measured at the back aperture of the objective). For pulsed interleaved excitation (66) of donor and acceptor, the power used for exciting the acceptor dye was adjusted to match the acceptor emission intensity to that of the donor (between 50 and 70 μW). Single-molecule FRET efficiency histograms were acquired from samples with protein concentrations between 50 pM and 100 pM. Trigger times for excitation pulses (repetition rate 20 MHz) and photon detection events were stored with 16 ps resolution.

For FRET-FCS, samples of labeled protein with a concentration of 1 nM were excited by the diode laser in continuous-wave mode at 100 μW. All measurements were performed in 50 mM sodium phosphate buffer, pH 7.0, 143 mM 2-mercaptoethanol (for photoprotection), 0.001% Tween 20 (for surface passivation) and GdmCl at the reported concentrations. Note that the FRET-FCS experiments reported here (i.e. above 0.5 M GdmCl) exhibit the pronounced anticorrelated component in the donor-acceptor crosscorrelation characteristic of donor-acceptor distance fluctuations, indicating that other contributions to the correlation function, such as PET quenching of the Alexa dyes, are negligible, as expected for this sequence separation (67).

Microfluidic mixing experiments. Microfluidic devices were fabricated using replica molding in poly(dimethylsiloxane) (PDMS) as described previously (51). The microfluidic device was mounted in a custom-made holder that allows the pressure driving the flow to be regulated individually for each channel. In the experiment (see Fig. 4A), we applied 13.8 kPa to the center inlet and 13.8 kPa to the side inlets, resulting in rapid dilution of the protein in high denaturant entering from the central inlet channel with buffer from the side inlet channels at a mixing ratio of 1:10. We acquired data at a position after the mixing region corresponding to 4 ms after mixing.

Ensemble time-correlated single-photon counting. High-resolution fluorescence lifetime decays were acquired with a custom-built instrument (68) in magic-angle configuration (69), using a supercontinuum laser source (SC-450-4, 20 MHz, Fianium, Southampton, U.K.) for excitation, resulting in a width of 80 ps for the instrument response function (full width at half-maximal intensity). Bimolecular quenching experiments were performed in 100 mM sodium phosphate buffer (pH 7.2) with 143 mM 2-mercaptoethanol, 0.001% (v/v) Tween 20, 25 nM of Atto-Oxa11, and the concentrations of tryptophan, GdmCl, and glycerol as specified.

Data Analysis

FRET efficiency and fluorescence lifetime histograms. Fluorescence bursts from individual molecules were identified by combining successive photons separated by inter-photon times of less than 150 μs and retaining the burst only if the total number of photons detected after donor excitation was greater than 50. Transfer efficiencies for each burst were calculated according to $E=n_A/(n_A+n_D)$, where n_D and n_A are the numbers of donor and acceptor photons, respectively, corrected for background, acceptor direct excitation, channel crosstalk, differences in detector efficiencies, and quantum yields of the dyes (70). The precision of the measured transfer efficiencies as estimated from multiple independent measurements is typically ±0.02 transfer efficiency units and thus comparable to or smaller than the data points reported in the figures, unless error bars are shown explicitly. Changes in refractive index caused by denaturant were

measured with a digital Abbe refractometer (Krüss, Germany) and were used to correct the Förster radius (R_0) for each sample.

Multiparameter detection allows us to exclude possible interfering artifacts, such as insufficient rotational averaging of the fluorophores or quenching of the dyes (71). The dependence of the fluorescence lifetimes on transfer efficiencies determined for each burst was compared with the behavior expected for fixed distances and for a chain sampling a broad distribution of distances. For a fixed distance, r, the mean donor lifetime in the presence of acceptor is given by $\tau_{DA}(r) = \tau_D(1-E(r))$, where τ_D is the donor lifetime in the absence of the acceptor, and $E(r) = 1/(1+r^6/R_0^6)$. For a dynamic chain with a dye-to-dye distance distribution, $P(r)$, the average donor lifetime is $\tau_{DA} = \int_0^\infty t\,I(t)\,dt \Big/ \int_0^\infty I(t)\,dt$ with $I(t) = I_0 \int_0^\infty P(r)\,e^{-t/\tau_{DA}(r)}dr$, where $I(t)$ is the time-resolved fluorescence emission intensity following donor excitation. Subpopulation-specific anisotropies were determined for both donor and acceptor, and values were found to vary between 0.23 and 0.19 for the donor and between 0.11 and 0.09 for the acceptor, consistent with values observed in ensemble measurements, and sufficiently low to assume as a good approximation for the orientational factor $\kappa^2 = 2/3$.

Quantifying distances from transfer efficiencies. Histograms of transfer efficiencies were fitted with three empirical peak functions, using a normal distribution for the donor-only and unfolded populations; the folded state was fitted to a log-normal distribution to account for the asymmetry of peaks at high transfer efficiency. Mean values of transfer efficiency, $\langle E \rangle$, corresponding to the unfolded population, were related to distance information by solving numerically

$$\langle E \rangle = \int E(r)P(r)dr\,, \qquad \text{(Eq. S1)}$$

where $P(r)$ is the distance distribution of an appropriate polymer model that accounts for the intramolecular distances sampled by the chain. We used three different distributions:

- the random walk (Gaussian) chain:

$$P_{Gauss}(r) = 4\pi r^2 \left(\frac{3}{2\pi R^2}\right)^{3/2} \exp\left(-\frac{3r^2}{2R^2}\right), \qquad \text{(Eq. S2)}$$

where R is the root-mean-square value of the interdye distance;

- the self-avoiding-walk (SAW):

$$P_{SAW}(r) = 4\pi r^2 \frac{0.278}{R^3}\left(\frac{r}{R}\right)^{0.28} \exp\left(-1.206\left(\frac{r}{R}\right)^{2.43}\right), \qquad \text{(Eq. S3)}$$

- and the Worm-like chain:

$$P_{WLC}(r) = Z \frac{4\pi\left(r/l_c\right)^2}{l_c\left[1-\left(r/l_c\right)^2\right]^{9/2}} \exp\left(\frac{-3l_c}{4l_p\left(1-\left(r/l_c\right)^2\right)}\right), \qquad \text{(Eq. S4)}$$

where Z is a normalization factor, l_c is the contour length, and l_p the persistence length of the chain. Eq. S1 was then solved either for R or l_p.

Finally, to account for the length of dye linkers and compare the experimental data with simulations, the root-mean-squared interdye distance R was rescaled according to $R_{m,n} = |m\text{-}n|^{0.5}/|m\text{-}n+2l|^{0.5}$ with $l = 4.5$ (43, 72). The same scaling law was used to estimate the intra-chain root-mean-square distance for the PET construct, $R_{47,64}=R_{7,64}$ $(64\text{-}47)^{0.5}/(64\text{-}7)^{0.5}$. It is interesting to compare the polymer models with the corresponding distance distributions from the MD simulation. In Fig. 2, although the variances of the distributions may differ by up to 30%, the ratio of the second moments from the polymer model and MD distributions are 1.01 for the GC and WLC and 0.96 for the SAW, whereas the ratio of the fourth moments is 0.86 for the GC, 0.83 for the WLC, and 0.78 for the SAW. Overall, simple polymer models capture the global properties of the internal distances sampled in the MD simulations well (see Fig. S1) but can of course not describe deviations due to specific local structure formation that can occur in atomistic models.

Reconfiguration times from FRET-FCS

Autocorrelation curves of acceptor and donor channels and cross-correlation curves between acceptor and donor channels were computed from the measurements and analyzed as described previously (10, 12, 61). The data were fitted over a time window of 4 μs according to

$$g_{ij}(\tau) = 1 + \frac{1}{N}\left(1 - c_{AB}e^{-\frac{t-t_0}{\tau_{AB}}}\right)\left(1 + c_{CD}e^{-\frac{t-t_0}{\tau_b}}\right)\left(1 + c_T e^{-\frac{t-t_0}{\tau_T}}\right), \qquad i, j = A, D \tag{S5}$$

where N is the mean number of molecules in the confocal volume, c_{AB}, c_{CD}, c_T are the amplitudes related to photon antibunching (AB), chain dynamics (CD), and triplet blinking of the dyes (T), and τ_{AB}, τ_{CD}, τ_T are the corresponding relaxation times. Assuming that chain dynamics can be described as a diffusive process in the potential of mean force derived from the sampled distance distribution $P(r)$ (16), we convert τ_{CD} to the reconfiguration time of the chain, τ_r (61). Since atomistic simulations are available only in the absence of denaturant, we employ the Gaussian chain model to obtain suitable distance distributions for all GdmCl concentrations investigated. Note that τ_{CD} and τ_r differ by only 5 to 10 % in the present case because the average distance is close to the Förster radius under all conditions (61). The analysis of FRET-FCS measurements was restricted to above 0.5 M GdmCl because of a static quenching component that becomes detectable at lower denaturant concentrations, as indicated by a correlated amplitude of the donor-acceptor crosscorrelation observed in microfluidic mixing experiments.

Separating internal friction and solvent components of the reconfiguration time.

According to the Rouse and Zimm model with internal friction (12, 36, 46), the reconfiguration time of the chain can be described as a sum of two components, τ_s and τ_i (see Eq. 1). To separate these two components, we adopted the following procedure. First, we studied the solvent viscosity dependence of τ_r at 6M GdmCl (Fig 3C, inset, purple). By linear extrapolation of τ_r to $\eta_s = 0$, we identified a considerable contribution of internal friction even at this high denaturant concentration, corresponding to $\tau_i(6\text{ M}) \approx 28\pm5$ ns and $\tau_s(6\text{ M}) \approx 35\pm7$ ns, similar in magnitude to the spectrin domains (10) and ubiquitin (72) under similar conditions. To quantify τ_s over the entire denaturant range, we rescaled τ_s(6M) by the values of $R^2\eta_s$ corresponding to each GdmCl concentration (10, 12) (Fig. 3C, blue line). Finally, to obtain an estimate of the internal friction contribution for all denaturant concentrations, we subtracted the rescaled τ_s from a polynomial interpolation of the measured reconfiguration times (Fig. 3C, orange line). We optimize the estimate by allowing the solvent and internal friction components in the model to be adjusted within the bounds of the propagated experimental errors and assuming that the internal friction remains constant above 6M GdmCl. As a consistency check, we studied the

viscosity dependence at 2M GdmCl (Fig 3C, inset, magenta). We found τ_l (2 M) ≈ 40±10 ns and τ_s (2 M) ≈ 10±5 ns, in line with the predictions from the Rouse model (see Fig. 3C).

Bimolecular dynamic quenching of Trp and ATTO Oxa11 from fluorescence lifetimes. The recorded fluorescence lifetime decays were fitted with single-exponential decays convolved with the instrument response function (IRF) obtained from the measurement of scattered laser light (50). The buffer contained 100 mM potassium phosphate pH 7.2, 143 mM 2-mercaptoethanol, and 0.001% Tween 20. A dye concentration of 25 nM was used for Oxa11.

PET-FCS measurements of bimolecular quenching between Trp and ATTO Oxa11. The static quenching rate of Oxa11 by Trp was obtained via bimolecular PET-FCS measurements of Oxa11 in the presence of a fixed concentration of Trp at varying GdmCl concentration. The dynamic quenching rate was obtained from the change in fluorescence lifetime of Oxa11 in the presence and absence of Trp at different concentrations of GdmCl, as reported in Fig. S6A. The fluorescence lifetime of Oxa11, τ_{Oxa11}, at a given Trp concentration, c_{Trp}, is related to the dynamic quenching rate via $k_{coll}^{dyn} = 1/\tau_{Oxa11}(c_{Trp}) - 1/\tau_{Oxa11}(0)$. A theoretical estimate of the bimolecular collision rate can be obtained from the Smoluchowski theory for diffusion-limited reactions:

$$k_{coll}^{theo} = 4\pi N_A (\mathrm{D}_{Trp} + \mathrm{D}_{Oxa11})(R_{Trp} + R_{Oxa11}) = (5 \pm 2) \cdot 10^9 \,\mathrm{M^{-1}s^{-1}} \,, \qquad \text{(Eq. S6)}$$

where we used D_{Trp} = 6.6·10^{-6} cm^2 s^{-1} and D_{Oxa11} = 2.8·10^{-6} cm^2 s^{-1} for the diffusion constants of Trp and Oxa11, respectively (50). Based on MD simulations (56), the center-to-center distance between Oxa11 and Trp, $R_{Trp} + R_{Oxa11}$, was previously estimated to be 0.7±0.3 nm (50). At a Trp concentration of 6.5 mM, k_{coll}^{theo} = (0.033 ± 0.013) ns^{-1}, very close to the value of k_{coll}^{dyn} observed in the absence of denaturant (Fig. S6B). Since the measured value is within the uncertainty of k_{coll}^{theo} (Fig. S6B, shaded band), the dynamic quenching rate is assumed to be a good experimental estimate for diffusion-limited contact formation rate between Oxa11 and Trp. However, with increasing GdmCl concentration, k_{coll}^{dyn} deviates from the trend expected if only the increase in solution viscosity is taken into account (Fig. S6B, dashed line), suggesting that GdmCl alters the quenching mechanism (possibly by restricting the accessibility of the two molecules due to preferential interactions with Oxa11 and Trp) and thus leads to an underestimate of the collision rate. We therefore obtain the value of the diffusion-limited collision rate independent of denaturant effects by rescaling the value observed at zero denaturant, $k_{coll}^{dyn}(0\mathrm{M})$, by the change in viscosity, i.e. $k_{coll}^{dyn*}(c_{GdmCl}) = k_{coll}^{dyn}(0\mathrm{M})\,\eta(0)/\eta(c_{GdmCl})$.

The bimolecular collision rates k_{coll}^{static} in the presence of 6.5 mM Trp were extracted by analyzing the amplitudes, c_b, and relaxation times, τ_b, of the PET-FCS curves as described in the main text (see section *Contact formation dynamics from PET-FCS*). Bimolecular collision times for the static and dynamic quenching processes can be obtained as the reciprocals of the corresponding rates, $1/k_{coll}^{static}$ and $1/k_{coll}^{dyn}$, respectively (Fig. S7E). Notably, the static quenching time is greater than the dynamic quenching time at all denaturant concentrations, indicating that static quenching is not diffusion-limited. From the ratios of k_{coll}^{static} and k_{coll}^{dyn} or k_{coll}^{dyn*}, respectively, we estimate the corresponding quenching efficiencies, ϕ or ϕ^*, of the reaction-limited contact formation process measured with PET-FCS experiments as a function of GdmCl concentration (see Fig. S7F). As discussed above, k_{coll}^{dyn} is likely to reflect not only the simple diffusional

collisions of dye and quencher but to contain contributions from shielding effects of GdmCl. We thus use ϕ^*, which is based on the viscosity-corrected rates, k_{coll}^{dyn*}, to estimate the efficiency of static quenching. Note, however, that ϕ and ϕ^* differ by less than 0.1 in the accessible GdmCl concentration range. This approach results in a value of $\phi^* \approx 50\%$ in the absence of denaturant, compatible with the values between 33% and 50% reported previously for similar oxazine dyes (50). The quenching efficiency decreases monotonically with increasing GdmCl concentration, reaching a value of ~20% at 3.5 M GdmCl (see Fig. 4G inset and SI).

We conducted analogous experiments in the presence of various concentrations of glycerol to investigate the impact of viscosity on the contact formation time and on the quenching efficiency. Based on the analysis of the measured amplitudes and quenching times, we found that the contact formation time is directly proportional to the change in solution viscosity in this case, suggesting that no further correction needs to be included for the quenching efficiency.

PET-FCS measurements of protein L W47C64 in the microfluidic mixer. For PET-FCS experiments in the microfluidic mixer, we took measurements ~4 ms after mixing, compared to folding times of ~25 ms to ~2 s for protein L in the GdmCl concentration range used here (73), corresponding to a fraction of unfolded protein between 92 and 100 %. The stability curve of the Oxa11-labeled protein, obtained by dividing the values of c_q measured at equilibrium by those observed in the microfluidic device (where the protein is completely unfolded), shows a midpoint of ~1.8 M GdmCl, very similar to the FRET-labeled variant (1.5 M). The similarity of the stability curves (Fig. 2C) provides additional confirmation that the protein is unfolded at the position where we observe it in the microfluidic device. A small decay component on the microsecond timescale is present even if the quenching Trp is exchanged to Phe in the protein sequence, and its amplitude increases linearly with increasing laser power. Therefore, this contribution is independent of chain dynamics and most likely due to residual triplet state blinking of Oxa11.

PET-FCS measurements of protein L W47C64 as a function of viscosity. Measurements of the contact formation rate in the presence of viscogens are challenging because increasing concentrations of viscogen decrease the amplitude of the correlation, affecting both the ratio k_+^{obs}/k_-^{obs} (see previous section) and the fraction of unfolded protein, f_u (by stabilizing the folded state). Measurements at high viscosity impair microfluidic mixing experiments owing to high backpressures that limit the concentration range of denaturant that we can investigate. Above 3.5 M GdmCl, correlation amplitudes are too small because GdmCl destabilizes the static complex; below 1.5 M GdmCl, correlation amplitudes are small because the protein is predominantly folded. Therefore, as a compromise between these two limits, we performed the measurements at 2M GdmCl with glycerol as a viscogen. Since the information contained in the quenching amplitude about f_u cannot be disentangled from the ratio of the k_+^{obs}/k_-^{obs} without additional information, we resorted to a different strategy: given the similar stabilities of the FRET and PET constructs (see Fig. 2), we investigated how viscogens affect the unfolded fraction of the FRET construct. f_u was quantified from the areas of the transfer efficiency peaks corresponding to the unfolded and folded population in single-molecule FRET experiments. We then performed measurements of the PET construct at the same concentrations of glycerol used in the FRET experiments, and by correcting for changes in f_u, we extracted τ_c as a function of viscosity. A linear fit of the viscosity dependence (36) yields $\tau_c = \tau_c^s + \tau_c^i$, where $\tau_c^s = 25 \pm 20$ ns and $\tau_c^i = 180 \pm 40$ ns (see Fig. S14).

Analysis of the MD simulations. Trajectories for protein L, Csp, and ProTα were simulated with the Amber 12 force field and the TIP4P-D water model by Piana *et al.* (31). Atomic

coordinates for the protein were saved with a 1-ns time resolution for a total length of 86 μs for protein L, 84 μs for Csp, and 10 μs for ProTα. Positions of C^{α} atoms were used to compute distances within the chain, $r_{m,n}^{sim}$ (see Fig. S1); positions of the backbone atoms were used to calculate the dihedral angles, ϕ and ψ. Formation of backbone hydrogen bonds and assignment of secondary structure were obtained using the DSSP algorithm implemented in CAMPARI (74). Salt bridges were identified using cutoff distances of 0.80 nm between the C^{γ} of Asp or the C^{δ} of Glu and the N^{ζ} of Lys or the C^{ζ} of Arg. Interactions between hydrophobic side chains were identified using cutoff distances of 0.90 nm between the C^{γ} of Val, Ile, Leu, Phe, Tyr, and Trp. Cutoff distance were chosen as in reference (14) to facilitate direct comparison. However, the choice of the cutoff distance mainly affects the number of salt bridges and hydrophobic interactions detected and has a relatively small effect on the average relaxation time, indicating that the relaxation times are robust with respect to the cutoff.

Relaxation times of distances, dihedral angles, and hydrogen bonds were obtained by integrating the corresponding time correlation functions, $C(\tau)$, according to $\int_0^{\tau_f} (C(\tau) - C(\tau_f)) / (C(0) - C(\tau_f))\, d\tau$. τ_f was chosen as the lag time at which the amplitude of the correlation function decayed to $1/e^2$ (Fig. S2) to focus on the dominant timescale of unfolded-state relaxation and to reduce the variability of the results due to a variation in integration time and slower dynamic components. Since these values are very similar across correlations of different quantities for the same protein (distances, hydrogen bonds, dihedral angles etc.), the largest τ_f of all correlations was chosen for each protein as the upper limit of integration. The chain reconfiguration time, τ_r, of the distance, r, between residues was calculated from the time correlation function of the distance, $C_r(\tau) = \langle r(t+\tau) r(t) \rangle_t \big/ \langle r(t)^2 \rangle_t$. The relaxation time for dihedral angles, τ_θ, was calculated by integrating the average of the correlation curves for the ϕ and ψ angles, $C_\phi(\tau) = \langle \phi(t+\tau)\phi(t) \rangle_t \big/ \langle \phi(t)^2 \rangle_t$ and $C_\psi(\tau) = \langle \psi(t+\tau)\psi(t) \rangle_t \big/ \langle \psi(t)^2 \rangle_t$. The relaxation time of hydrogen bonds was obtained from the correlation function $C_{hb}(\tau) = \langle u(t+\tau)u(t) \rangle_t \big/ \langle u(t)^2 \rangle_t$, where $u(t)$ is a function specific to each amino acid and is equal to zero if no hydrogen bonds are formed and equal to 1 if hydrogen bonds are formed at time t. The hydrogen bond map was constructed by averaging the number of hydrogen bonds between each amino acid pair per nanosecond along the trajectory. Similarly, the relaxation times of salt bridges and hydrophobic interactions were obtained from the correlation functions $C_h(\tau) = \langle h(t+\tau)h(t) \rangle_t \big/ \langle h(t)^2 \rangle_t$ and $C_{sb}(\tau) = \langle s(t+\tau)s(t) \rangle_t \big/ \langle s(t)^2 \rangle_t$, where $h(t)$ and $s(t)$ are functions specific to each amino acid pair and are equal to zero if no hydrophobic interaction (h) or salt bridge (s) is formed, and equal to 1 if the salt bridge or hydrophobic interaction is occurring at time t.

The contact formation time was calculated as $\tau_c = \int_0^{\infty} S(t)dt$, where $S(t)$ is the survival probability of the unquenched state (75):

$$S(t) = \left\langle \exp\left(-\int_{t_0}^{t_0+t} k_0 \theta\left(R_c - r_{47,64}(\tau)\right) d\tau \right) f_q \right\rangle_{t_0} \Big/ \left\langle f_q \right\rangle_{t_0} . \qquad \text{Eq. (S7)}$$

$k(r_{47,64}) = k_0 \theta\left(R_c - r_{47,64}\right)$ describes the distance dependence of the quenching rate between positions 47 and 64 (where Trp and Oxa11 are located), approximated by the Heavyside step function, θ; k_0 is chosen sufficiently large to recover τ_c to be diffusion-limited (i.e., independent

of k); $f_q = \theta\left(r_{47,64}\left(t_0\right) - R_c\right)$ is a correction for the (small) fraction of conformations that are in contact at time t_0; the contact formation radius, R_c, is the only adjustable parameter. The contact formation time map (Fig. S11 D-F) was constructed assuming R_c = 0.8 nm and computing contact formation times for all pairs of amino acids within the chain.

For Csp and protein L, errors for all calculated quantities were assigned by repeating the analysis on 10-μs segments of the trajectories and calculating mean and standard deviation of the quantity of interest. For ProTα, since the MD simulation is shorter than 10 μs, the trajectory was split in two, and mean and standard deviation of the quantities of interest were computed for each half. Asymmetric error bands reflect the difference between the value obtained by analyzing the whole trajectory (reported value) or averaging over shorter segments (center of the error interval).

nsFCS correlations from MD simulations. Autocorrelations for the donor and acceptor channels and crosscorrelations were calculated from the simulations (see Fig. 3B) following the approach described previously (67, 76). The photophysics of FRET are described with a kinetic model with three states, corresponding to the ground state (DA), the excited state of the donor (D*A), and the excited state of the acceptor (DA*). The time evolution of the state populations, $\mathbf{p}(t)$, is then given by the rate equation $\mathrm{d}\mathbf{p}/\mathrm{d}t = \mathbf{K}\mathbf{p}(t)$, where $\mathbf{p}$ is normalized ($\mathbf{1}^{\mathrm{T}}\mathbf{p} = 1$). $\mathbf{K}$ is

$$\mathbf{K} = \begin{pmatrix} -k_{exD} - k_{exA} & k_D & k_A \\ k_{exD} & -k_D - k_F(r) & 0 \\ k_{exA} & k_F(r) & -k_A \end{pmatrix}, \qquad \text{Eq. (S8)}$$

where k_{exD} and k_{exA} are the excitation rates for the donor and acceptor; k_{D} and k_{A} are the relaxation rates to the ground state; and $k_F(r)$ is the energy transfer rate given by $k_F(r) = k_D (R_0/r)^6$. The distance, r, is obtained from the MD trajectory as a function of time. Since the simulations have a time resolution of only 1 ns, each time step is subdivided into 10 substeps, where the distance is assumed to be constant. With the detection matrices, $\mathbf{V}_{\mathrm{D}}$ and $\mathbf{V}_{\mathrm{A}}$, which contain the radiative rate constants for the monitored transitions,

$$\mathbf{V}_D = \begin{pmatrix} 0 & k_D & 0 \\ 0 & 0 & 0 \\ 0 & 0 & 0 \end{pmatrix}, \mathbf{V}_A = \begin{pmatrix} 0 & 0 & k_A \\ 0 & 0 & 0 \\ 0 & 0 & 0 \end{pmatrix}, \qquad \text{Eq. (S9)}$$

the fluorescence intensity correlations can be computed as (i = A, D, j = A, D)

$$g_{ij}(\tau) = \frac{\mathbf{1}^T \mathbf{V}_i e^{\mathbf{K}\tau} \mathbf{V}_j \mathbf{p}_{ss}}{\left(\mathbf{1}^T \mathbf{V}_i \mathbf{p}_{ss}\right)\left(\mathbf{1}^T \mathbf{V}_j \mathbf{p}_{ss}\right)}. \qquad \text{Eq. (S10)}$$

To account for spectral cross-talk, direct excitation, and the presence of a donor-only species, the correlation is rewritten as a sum of weighted contributions:

$$G_{ij}(\tau) = 1 + a_{ij} \frac{c_d B_{d,i} B_{d,j} g^d_{i,j}(\tau) + c_f B_{f,i} B_{f,j} g^f_{i,j}(\tau)}{\left(c_d B_{d,i} + c_f B_{f,i}\right)\left(c_d B_{d,j} + c_f B_{f,j}\right)}, \qquad \text{Eq. (S11)}$$

where f and d are the FRET and donor-only populations, respectively. The brightness values are computed as previously (67), with $B_{d,D} = 1$, $B_{f,D} = 1\text{-}E$, $B_{f,A} = \gamma\,(E + \alpha) + \beta\,(1 - E)$, and $B_{d,A}$

= β. The ratio of detection efficiencies of donor and acceptor is $\gamma = 1.13$, the direct excitation of the acceptor is $\alpha = 0.048$, and the crosstalk of donor emission detected in the acceptor channel is $\beta = 0.066$. The relative abundances, c_d and c_f, are estimated from the corresponding transfer efficiency histogram to be ~50%. The overall amplitude, a_{ij}, is used as an adjustable parameter.

Tables.

protein L wild type	1 10 20 30 40 MEEVTIKANL IFANGSTQTA EFKGTFEKAT SEAYAYADTL 50 60 64 KKDNGE**W**TVD VADKGYTLNI KFAG
FRET variant (C7-C64)	1 10 20 30 40 MAHHHHHHSAALEVLFQ/GP MEEVTI**C**ANL IFANGSTQTA EFKGTFEKAT SEAYAYADTL 50 60 64 KKDNGE**W**TVD VADKGYTLNI KFA**C**
PET variant (C64)	1 10 20 30 40 MAHHHHHHSAALEVLFQ/GP MEEVTIKANL IFANGSTQTA EFKGTFEKAT SEAYAYADTL 50 60 64 KKDNGE**W**TVD VADKGYTLNI KFA**C**
control variant (F47-C64)	1 10 20 30 40 MAHHHHHHSAALEVLFQ/GP MEEVTIKANL IFANGSTQTA EFKGTFEKAT SEAYAYADTL 50 60 64 KKDNGE**F**TVD VADKGYTLNI KFA**C**

Table S1. Amino acid sequences of protein L used in this study compared with the wild type sequence. Cys residues (in red) were introduced for labeling with fluorescent dyes (Alexa 488 and Alexa 594 for FRET based experiments, OXA11 for PET-FCS experiments). For the FRET construct, labeling positions were selected based on previous single-molecule FRET experiments on protein L (37, 38) with the aim of optimizing the separation between folded and unfolded state transfer efficiencies. For measuring contact formation by PET (49), we prepared a single-cysteine variant, G64C, and labeled it with ATTO Oxa11, which is quenched when a complex with the natural tryptophan, W47 (green), is formed. The same Trp residue that acts as a quencher of Oxa11 in the PET construct was used in previous contact formation experiments based on triplet quenching of Trp by Cys (W47-T57C) (18); however, we increased the probe-quencher separation from 10 to 18 amino acids to reduce the relative influence of the Oxa11 linker on the observed dynamics. In the control construct for the PET experiments, Trp is replaced by Phe.

SI Figures

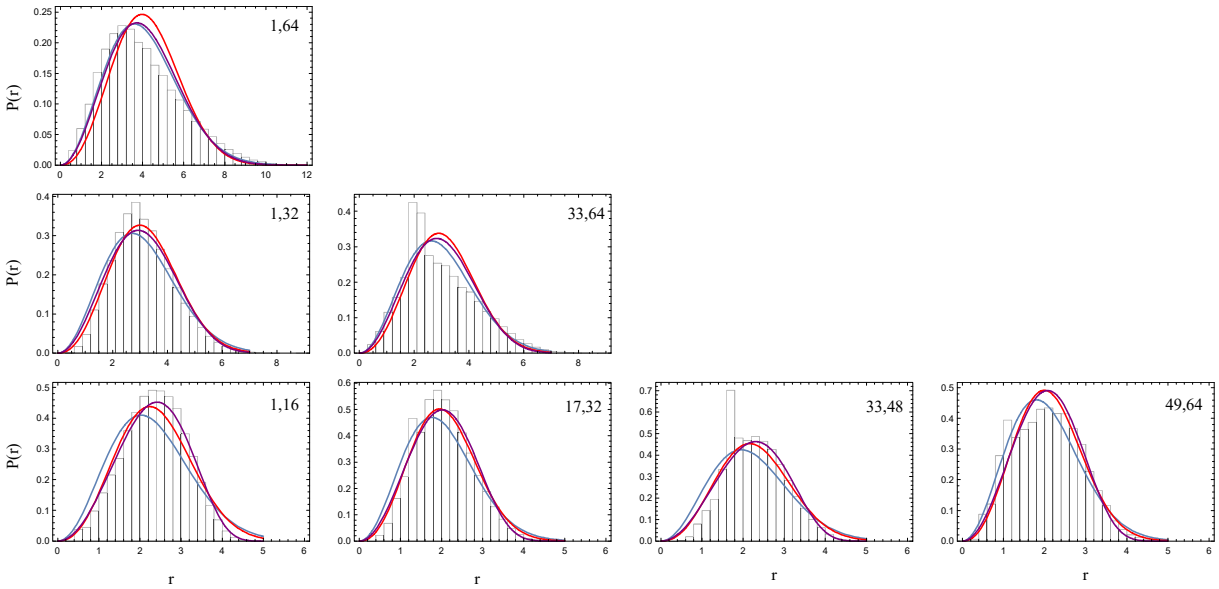

Figure S1. Comparison of distance distributions in MD simulations and polymer models. Distribution of distances between residues *m* and *n* (given in upper right corner of each panel) from the MD simulation of unfolded protein L (31) compared to the distance distributions for a Gaussian chain (blue), a self-avoiding-walk (red) and a worm-like chain (purple) with the same root-mean-square distances as the distributions from the simulations to illustrate the level of agreement between atomistic simulations and polymer models.

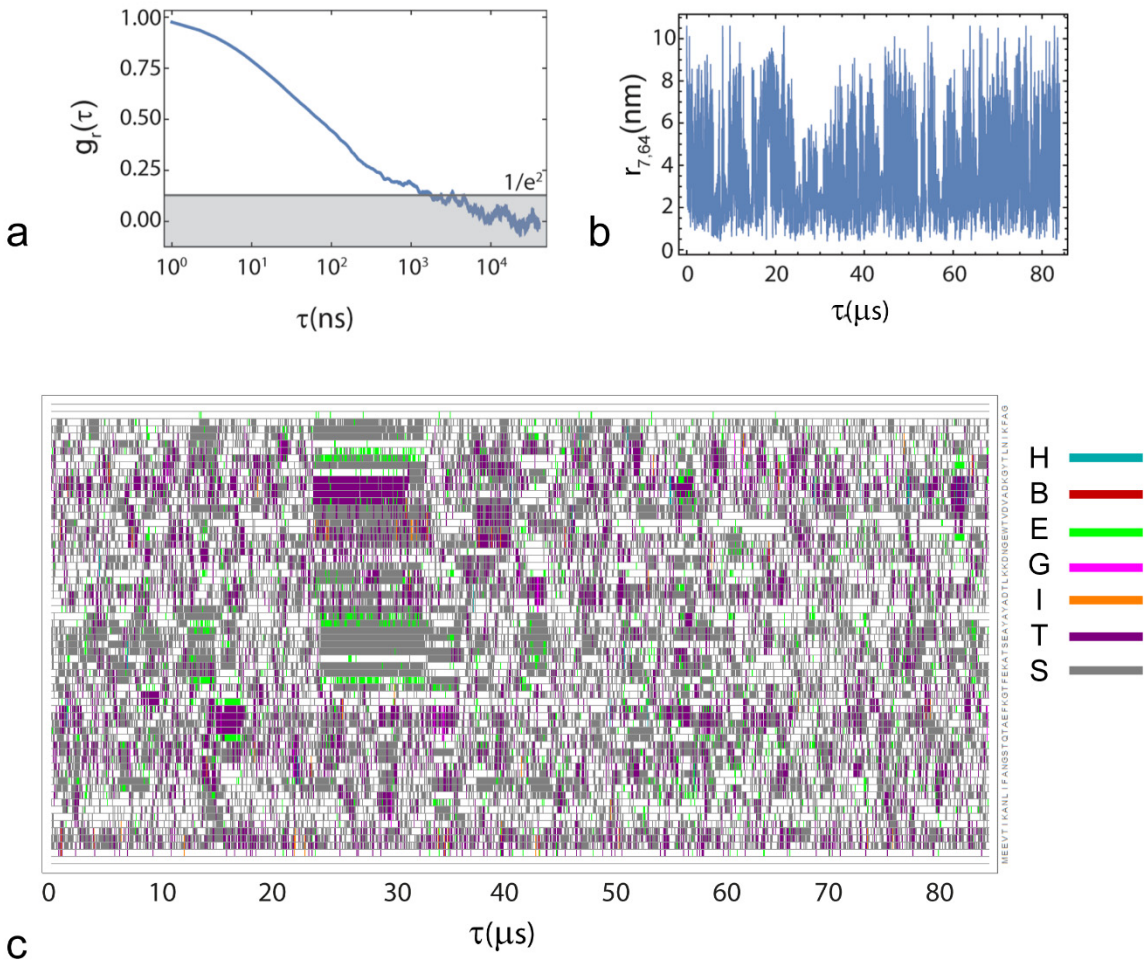

Figure S2. Correlation curve for the distance $r_{7,64}$, the corresponding distance trajectory, and secondary structure assignment from the MD simulation of unfolded protein L. (a) To extract the dominant timescale of chain reconfiguration, the analysis was restricted to the time range corresponding to amplitudes greater than $1/e^2$. (b) Trajectory of the distance $r_{7,64}$. (c) Assignment of secondary structure according to the DSSP algorithm (77) (H: α-helix, B: isolated β-bridge, E: extended/strand, G: 3-helix, I: 5-helix, T: hydrogen-bonded turn, S: bend). Slow dynamics on the timescale of several microseconds reflects the formation of short elements, especially bends, turns, and strands.

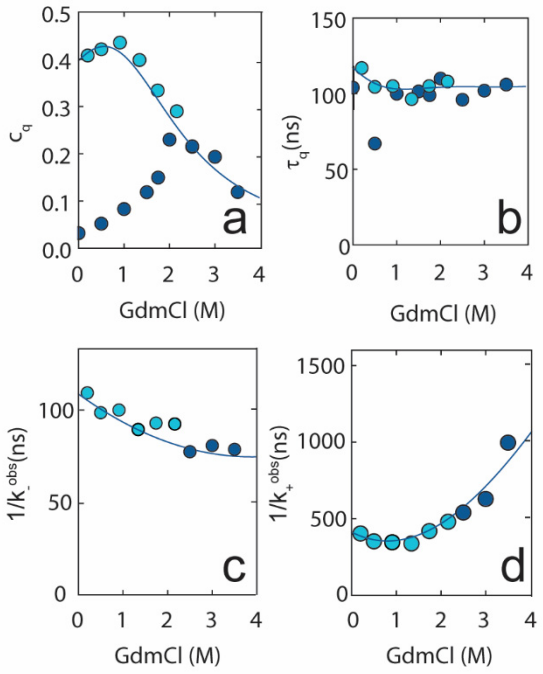

Figure S3. **Analysis of PET-FCS curves for unfolded protein L.** (A-B) Amplitude, c_q, and relaxation time, τ_q, of the quenching component as measured in the microfluidic device (light blue filled circles) and in equilibrium experiments (dark blue filled circles). Lines are polynomial fits of the data used for interpolation. (C-D) Reciprocal of the observed relaxation rates of forming and breaking the Trp-ATTO Oxa11 complex, k_+^{obs} and k_-^{obs}, respectively, as obtained from c_q and τ_q. Lines are obtained from the polynomial fits of c_q and τ_q.

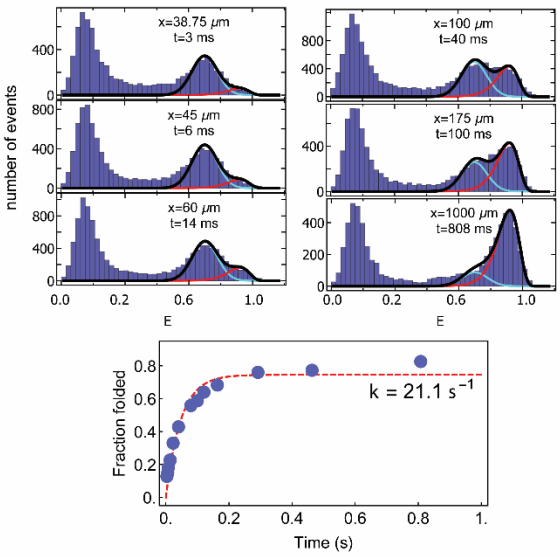

Figure S4. **Folding rate measured in the microfluidic mixing device.** Transfer efficiency histograms of protein L measured along the observation channel of the microfluidic device at different times (i.e. positions) after the solution is rapidly diluted from 3 M GdmCl to 0.3 M GdmCl with buffer solution (50 mM sodium phosphate pH 7.0). The fraction of folded protein increases with a rate of 21 ± 3 s^{-1}.

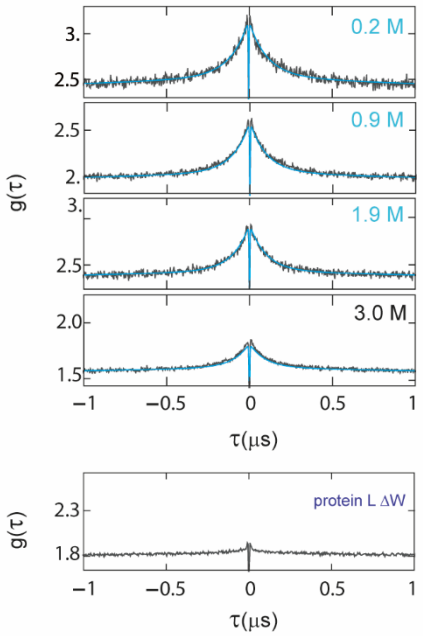

Figure S5. **PET-FCS of unfolded protein L.** (A) PET-FCS curves of unfolded protein L between -1 μs and 1 μs at different GdmCl concentrations. The fast correlated decay on the nanosecond timescale reports on the quenching process, and the amplitude is directly linked to the fraction of unfolded protein and to the stability of the complex. (B) PET-FCS of the control construct of protein L, where the quenching Trp is replaced by Phe (Table S1). The amplitude of the resulting correlation is less than 10% of the amplitude observed in 3.0 M GdmCl.

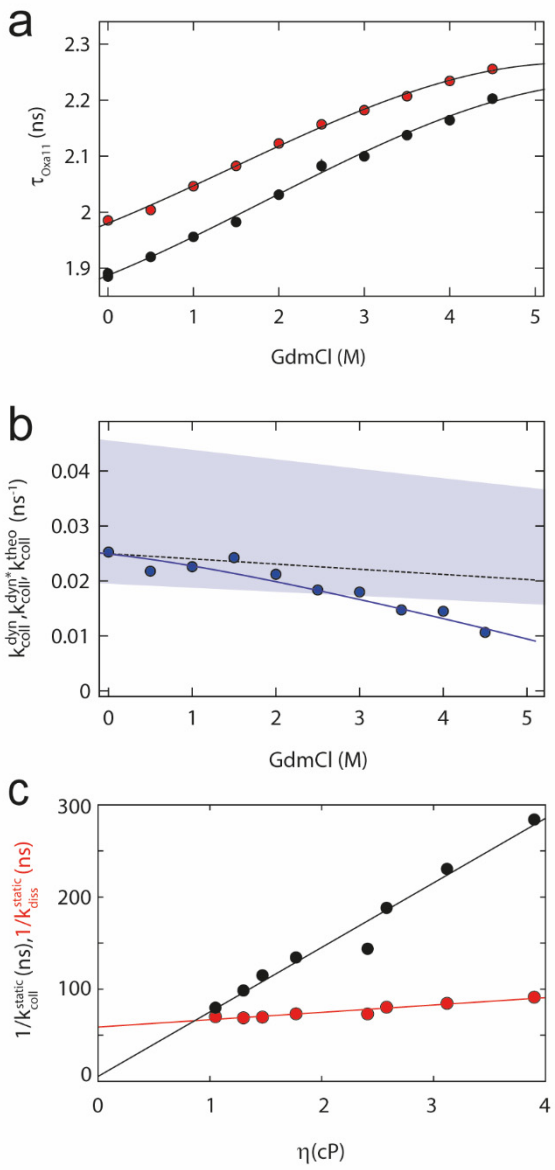

Figure S6. Bimolecular dynamic quenching experiments. (A) ATTO Oxa11 fluorescence lifetime in the presence (black filled circles) and absence (red filled circles) of 6.5 mM Trp as a function of GdmCl concentration. The solid line is a third-order polynomial used for interpolation. (B) Bimolecular collision rates, k_{coll}^{dyn} and k_{coll}^{dyn*}, from fluorescence lifetime-based dynamic quenching experiments (circles) compared to the theoretical estimate k_{coll}^{theo} based on Eq. S6, including changes in solvent viscosity (dashed line). The gray band shows the range of the theoretically expected bimolecular collision rate, based on the uncertainty of the contact radius between Oxa11 and Trp (see Eq. S6 and SI Text, *PET-FCS measurements of bimolecular quenching between Trp and ATTO Oxa11*). (C) Solvent viscosity (η) dependence of the bimolecular quenching rate for the formation and dissociation of the static complex, $1/k_{coll}^{static}$ and $1/k_{diss}^{static}$, respectively, in 100 mM sodium phosphate buffer. The inverse of the rate of complex formation is directly proportional to solvent viscosity, whereas the rate of complex dissociation is much less sensitive to viscosity.

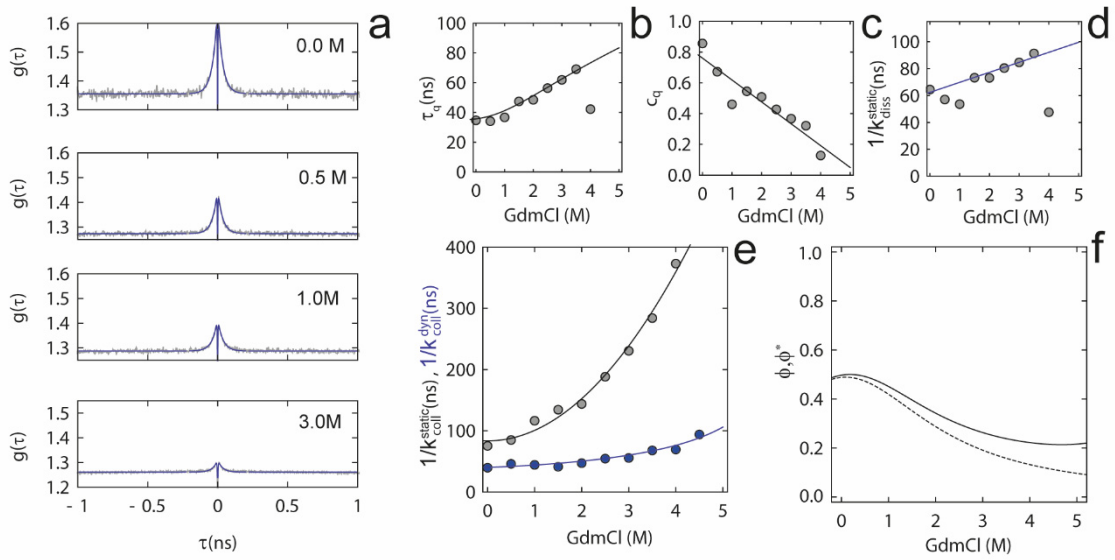

Figure S7. Denaturant dependence of bimolecular PET quenching. (A) Representative PET-FCS curves for bimolecular quenching of free ATTO Oxa11 by 6.5 mM Trp as a function of GdmCl concentration. (B-C) Quenching amplitude, c_q, and decay time, τ_q, as a function of GdmCl concentration. Above 3.5 M GdmCl, c_q becomes too small to be fit reliably. (D) Observed dissociation time of the static Oxa11-Trp complex, $1/k_{diss}^{static}$, as a function of denaturant. (E) Comparison between the bimolecular collision times measured via dynamic quenching, $1/k_{coll}^{dyn}$, (blue filled circles) and static quenching, $1/k_{coll}^{static}$, (gray filled circles). (F) Efficiency of static quenching, ϕ, estimated from the ratio $k_{coll}^{static}/k_{coll}^{dyn}$ using the measured values (solid line), or ϕ^*, using k_{coll}^{dyn} at 0 M GdmCl corrected for the change in solution viscosity (dashed line; cf. dashed line in Fig. S6b).

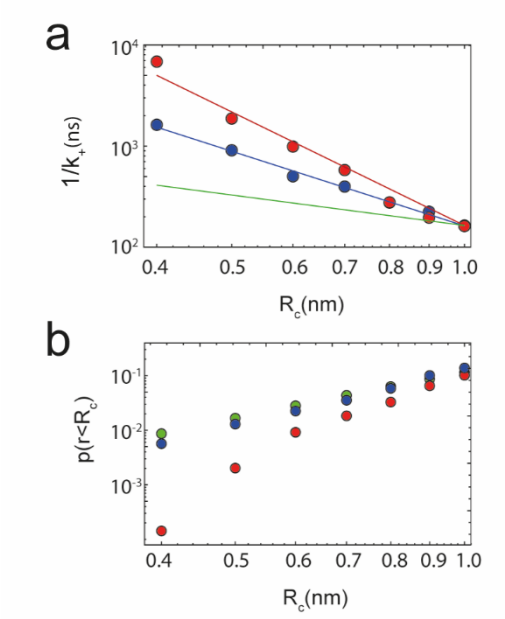

Figure S8. Dependence of the contact formation time, $1/k_+$, on the contact radius, R_c, between the quenching probes for protein L. (A) Contact times between W47 and G64 as calculated from the MD simulation of unfolded protein L (31) according to Eq. S7 for the distance between the C^α atoms of tryptophan and glycine (red filled circles), and between the center of mass of the tryptophan indole ring and the glycine C^α (blue filled circles). Contact times thus exhibit a stronger dependence on R_c than expected from Eq. 2 (green line). (B) Fraction of configurations with distances below R_c for the two cases shown in (A) (red and blue) compared to a Gaussian chain (green). The fraction based on the distance between the tryptophan indole ring and the glycine C^α approaches the trend expected for a Gaussian chain.

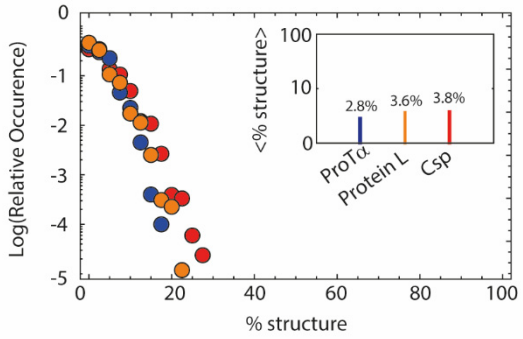

Figure S9. Secondary structure content from MD simulations of unfolded proteins. Relative occurrence of trajectory snapshots containing a specific percentage of residual secondary structure as assigned by the DSSP algorithm (74, 77). Similar values are observed for unfolded Csp (red), protein L (orange), and ProTα (blue). Inset: average percentage of residual secondary structure estimated from the entire trajectory.

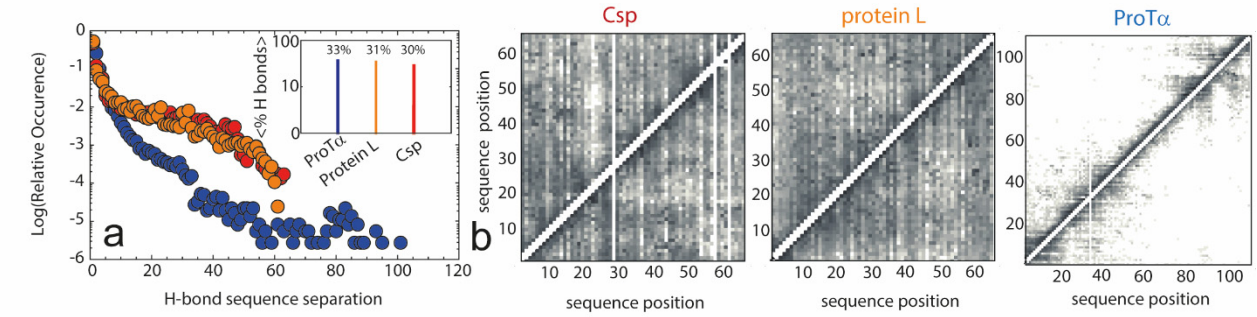

Figure S10. Hydrogen bond formation in unfolded proteins from MD simulations. (A) Occurrence of backbone hydrogen bonds as a function of sequence separation for unfolded Csp (red), protein L (orange), and ProTα (blue) based on the MD simulations (31) and identified using the DSSP algorithm (77). (A, inset) Average percentage of backbone hydrogen bonds present in each snapshot of the MD simulations (relative to all backbone hydrogen bonds identified by DSSP). (B) Map of the occurrence of hydrogen bonds between two amino acids in the MD trajectory (increasing probability from white to dark grey; same scale for all panels).

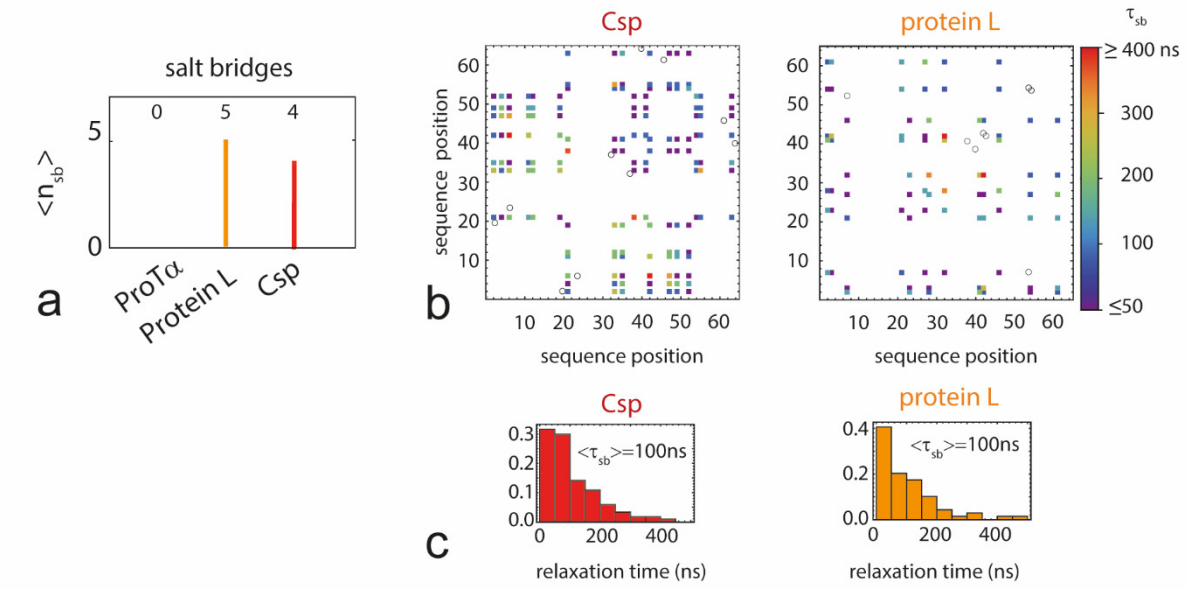

Figure S11. Formation of salt bridges in unfolded proteins from MD simulations. (a) Comparison of the average number of salt bridges per snapshot for ProTα, protein L, and Csp, assuming a cutoff distance of 0.8 nm (see SI Materials and Methods). Note that no salt bridges are detected in the simulation of ProTα. (b) Maps of salt bridges formed during the simulation, colored according to the corresponding relaxation time, τ_{sb}, of the correlation function C_{sb} (see SI Materials and Methods). Black circles correspond to salt bridges found in the native structure. (c) Distributions and mean values of τ_{sb} for protein L and Csp.

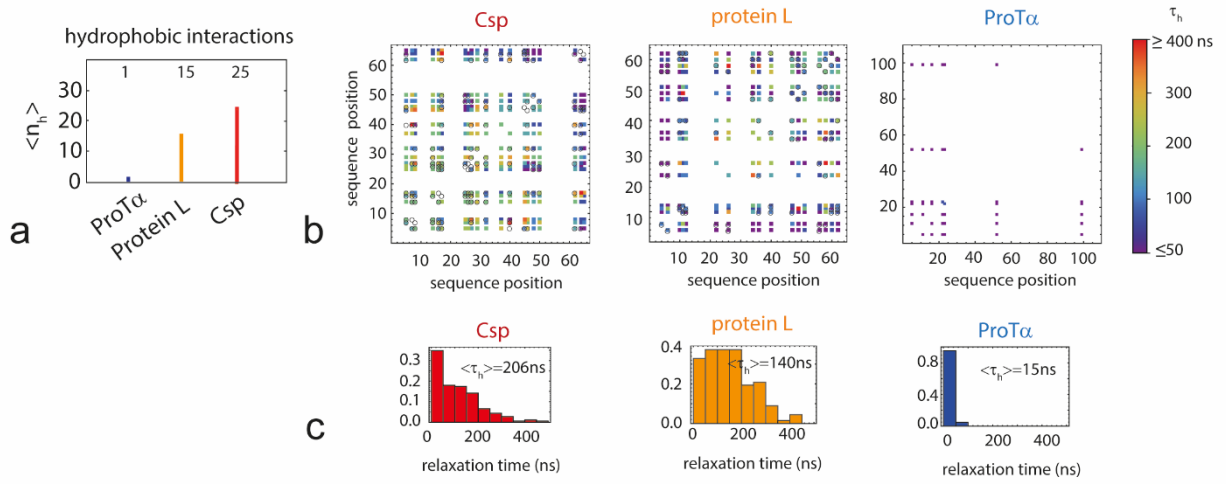

Figure S12. Formation of hydrophobic interactions in unfolded proteins from MD simulations. (a) Comparison of the average number of hydrophobic interactions between amino acid pairs per snapshot for ProTα, protein L, and Csp, using a cutoff distance of 0.9 nm (see SI Materials and Methods). (b) Maps of hydrophobic interactions between amino acids pairs, colored according to the corresponding relaxation time, τ_h, of the correlation function C_h (see SI Materials and Methods). Black circles correspond to hydrophobic interactions in the native structure. (c) Distributions and mean values of τ_h for ProTα, protein L and Csp.

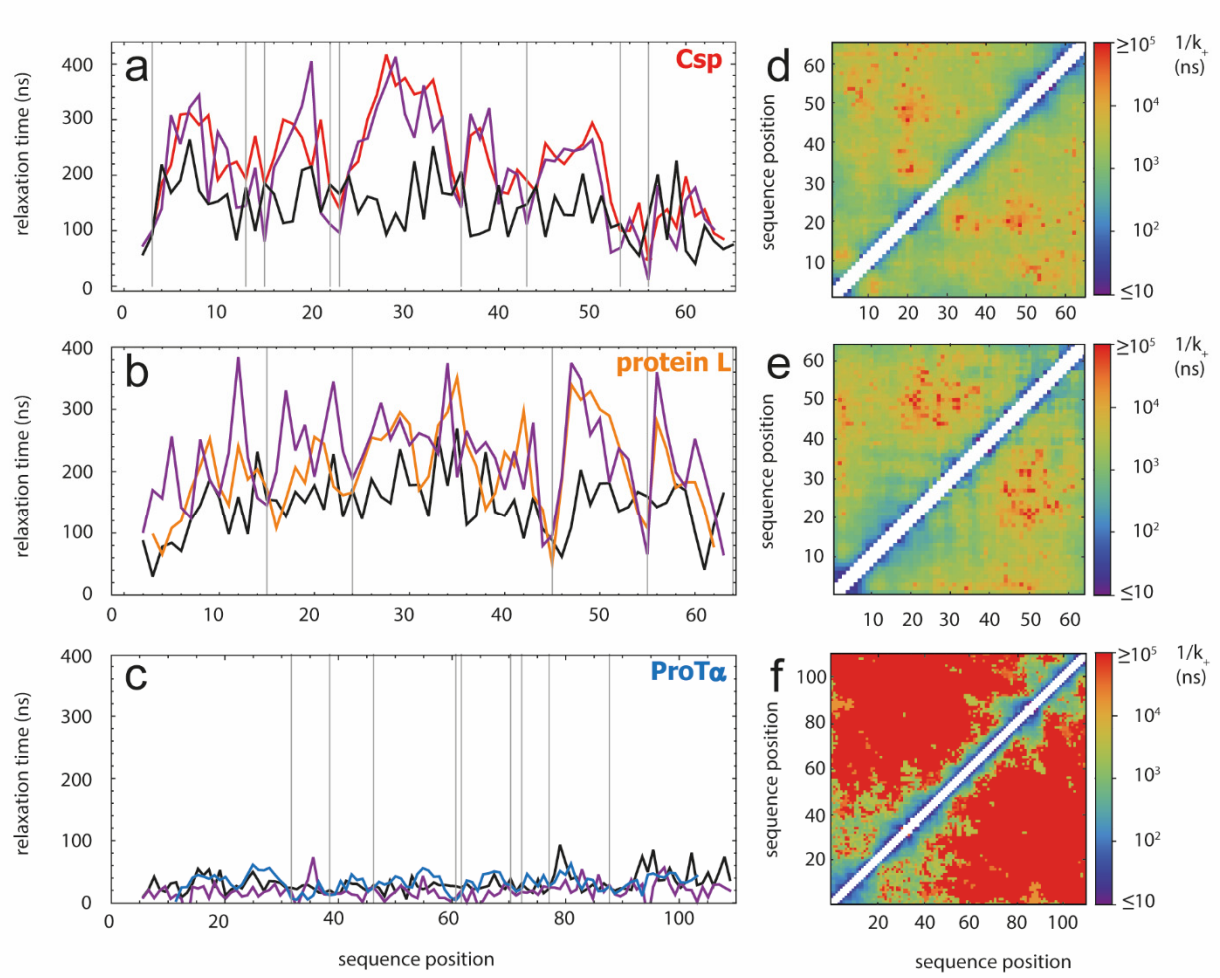

Figure S13. Dynamics of unfolded proteins from MD simulations. (A, B, C) Comparison of relaxation times extracted from the MD simulations (see SI) for the formation of backbone hydrogen bonds between a specific amino acid and the rest of the chain (black line), for the rotation of dihedral angles (purple line), and for the reconfiguration of intrasegment distances of 5-residue segments (approximately a Kuhn segment) for unfolded Csp (red), protein L (orange), and ProTα (blue). Vertical gray lines correspond to the position of glycine residues in the sequence. (D,E,F) Maps of contact formation times for unfolded Csp, protein L, and ProTα.

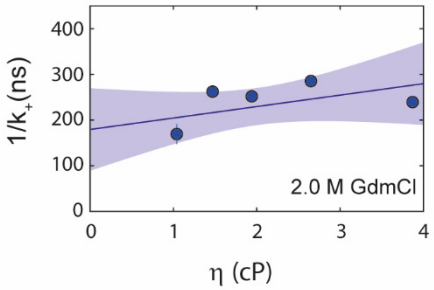

Figure S14. Viscosity dependence of contact formation. Viscosity dependence of the contact formation time, τ_c, in unfolded protein L at 2 M GdmCl as estimated from PET experiments. A linear fit to the data results in $1/k_+ = 1/k_+^s \eta/\eta_0 + 1/k_+^i$ with $1/k_+^i = 180 \pm 40$ ns and $1/k_+^s = 25 \pm 20$ ns, consistent with Eq. 2 when using $R_{47,64} = 4.9$ nm (Fig. 2B), $R_c = 0.8$ nm, and $\tau_i = 42$ ns (see main text). The shaded area corresponds to the 90% confidence interval of the fit.

Supporting references

1. Bryngelson JD, Onuchic JN, Socci ND, & Wolynes PG (1995) Funnels, pathways, and the energy landscape of protein folding: a synthesis. *Proteins* 21:167-195.
2. Dill KA & Chan HS (1997) From Levinthal to pathways to funnels. *Nat. Struct. Biol.* 4:10-19.
3. Camacho CJ & Thirumalai D (1993) Kinetics and Thermodynamics of Folding in Model Proteins. *Proc. Natl. Acad. Sci. USA* 90:6369-6372.
4. Hänggi P, Talkner P, & Borkovec M (1990) Reaction-Rate Theory - 50 Years after Kramers. *Rev. Mod. Phys.* 62:251-341.
5. Pabit SA, Roder H, & Hagen SJ (2004) Internal friction controls the speed of protein folding from a compact configuration. *Biochemistry* 43:12532-12538.
6. Cellmer T, Henry ER, Hofrichter J, & Eaton WA (2008) Measuring internal friction of an ultrafast-folding protein. *Proc. Natl. Acad. Sci. USA* 105:18320-18325.
7. Plaxco KW & Baker D (1998) Limited internal friction in the rate-limiting step of a two-state protein folding reaction. *Proc. Natl. Acad. Sci. USA* 95:13591-13596.
8. Qiu LL & Hagen SJ (2004) Internal friction in the ultrafast folding of the tryptophan cage. *Chem. Phys.* 307:243-249.
9. Ansari A, Jones CM, Henry ER, Hofrichter J, & Eaton WA (1992) The Role of Solvent Viscosity in the Dynamics of Protein Conformational-Changes. *Science* 256:1796-1798.
10. Borgia A*, et al.* (2012) Localizing Internal Friction along the Reaction Coordinate of Protein Folding by Combining Ensemble and Single Molecule Fluorescence Spectroscopy. *Nat. Commun.* 2:1195.
11. Wensley BG*, et al.* (2010) Experimental evidence for a frustrated energy landscape in a three-helix-bundle protein family. *Nature* 463:685-U122.
12. Soranno A*, et al.* (2012) Quantifying internal friction in unfolded and intrinsically disordered proteins with single-molecule spectroscopy. *Proc. Natl. Acad. Sci. USA* 109:17800-17806.
13. Hagen SJ (2010) Solvent viscosity and friction in protein folding dynamics. *Curr. Protein Pept. Sci.* 11:385-395.
14. Chung HS, Piana-Agostinetti S, Shaw DE, & Eaton WA (2015) Structural origin of slow diffusion in protein folding. *Science* 349:1504-1510.
15. Frauenfelder H & Wolynes PG (1985) Rate theories and puzzles of hemeprotein kinetics. *Science* 229:337-345.
16. Nettels D, Gopich IV, Hoffmann A, & Schuler B (2007) Ultrafast dynamics of protein collapse from single-molecule photon statistics. *Proc. Natl. Acad. Sci. USA* 104:2655-2660.
17. Neuweiler H, Johnson CM, & Fersht AR (2009) Direct observation of ultrafast folding and denatured state dynamics in single protein molecules. *Proc. Natl. Acad. Sci. USA* 106:18569-18574.
18. Waldauer SA, Bakajin O, & Lapidus LJ (2010) Extremely slow intramolecular diffusion in unfolded protein L. *Proc. Natl. Acad. Sci. USA* 107:13713-13717.
19. Schulz JCF, Schmidt L, Best RB, Dzubiella J, & Netz RR (2012) Peptide Chain Dynamics in Light and Heavy Water: Zooming in on Internal Friction. *J. Am. Chem. Soc.* 134:6273-6279.
20. de Sancho D, Sirur A, & Best RB (2014) Molecular origins of internal friction effects on protein-folding rates. *Nat. Commun.* 5.
21. Echeverria I, Makarov DE, & Papoian GA (2014) Concerted Dihedral Rotations Give Rise to Internal Friction in Unfolded Proteins. *J. Am. Chem. Soc.* 136:8708-8713.

22. Sizemore SM, Cope SM, Roy A, Ghirlanda G, & Vaiana SM (2015) Slow Internal Dynamics and Charge Expansion in the Disordered Protein CGRP: A Comparison with Amylin. *Biophys. J.* 109:1038-1048.
23. Schuler B, Hofmann H, Nettels D, & Soranno A (2016) Single-molecule FRET spectroscopy and the polymer physics of unfolded and intrinsically disordered proteins. *Annu. Rev. Biophys.* DOI: 10.1146/annurev-biophys-062215-010915.
24. Zheng WW, De Sancho D, Hoppe T, & Best RB (2015) Dependence of Internal Friction on Folding Mechanism. *J. Am. Chem. Soc.* 137:3283-3290.
25. Zheng WW, de Sancho D, & Best RB (2016) Modulation of Folding Internal Friction by Local and Global Barrier Heights. *J. Phys. Chem. Lett.* 7:1028-1034.
26. Portman JJ, Takada S, & Wolynes PG (2001) Microscopic theory of protein folding rates. II. Local reaction coordinates and chain dynamics. *J. Chem. Phys.* 114:5082-5096.
27. Hofmann H*, et al.* (2014) Role of denatured-state properties in chaperonin action probed by single-molecule spectroscopy. *Biophys. J.* 107:2891-2902.
28. Zerze GH, Mittal J, & Best RB (2016) Diffusive Dynamics of Contact Formation in Disordered Polypeptides. *Phys. Rev. Lett.* 116:068102.
29. Shaw DE*, et al.* (2009) Millisecond-Scale Molecular Dynamics Simulations on Anton. *Proceedings of the Conference on High Performance Computing Networking, Storage and Analysis*.
30. Voelz VA, Singh VR, Wedemeyer WJ, Lapidus LJ, & Pande VS (2010) Unfolded-state dynamics and structure of protein L characterized by simulation and experiment. *J. Am. Chem. Soc.* 132:4702-4709.
31. Piana S, Donchev AG, Robustelli P, & Shaw DE (2015) Water dispersion interactions strongly influence simulated structural properties of disordered protein States. *J Phys Chem B* 119:5113-5123.
32. Best RB, Zheng W, & Mittal J (2014) Balanced Protein-Water Interactions Improve Properties of Disordered Proteins and Non-Specific Protein Association. *J. Chem. Theory Comput.* 10:5113-5124.
33. Vitalis A & Pappu RV (2009) ABSINTH: a new continuum solvation model for simulations of polypeptides in aqueous solutions. *J. Comput. Chem.* 30:673-699.
34. Nerenberg PS, Jo B, So C, Tripathy A, & Head-Gordon T (2012) Optimizing solute-water van der Waals interactions to reproduce solvation free energies. *J. Phys. Chem. B* 116:4524-4534.
35. Huang J*, et al.* (2017) CHARMM36m: an improved force field for folded and intrinsically disordered proteins. *Nat. Methods* 14:71-73.
36. Cheng RR, Hawk AT, & Makarov DE (2013) Exploring the role of internal friction in the dynamics of unfolded proteins using simple polymer models. *J. Chem. Phys.* 138.
37. Sherman E & Haran G (2006) Coil-globule transition in the denatured state of a small protein. *Proc. Natl. Acad. Sci. USA* 103:11539-11543.
38. Merchant KA, Best RB, Louis JM, Gopich IV, & Eaton WA (2007) Characterizing the unfolded states of proteins using single-molecule FRET spectroscopy and molecular simulations. *Proc. Natl. Acad. Sci. USA* 104:1528-1533.
39. Voelz VA*, et al.* (2012) Slow Unfolded-State Structuring in Acyl-CoA Binding Protein Folding Revealed by Simulation and Experiment. *J. Am. Chem. Soc.* 134:12565-12577.
40. Haran G (2012) How, when and why proteins collapse: the relation to folding. *Curr. Opin. Struct. Biol.* 22:14-20.
41. Borgia A*, et al.* (2016) Consistent View of Polypeptide Chain Expansion in Chemical Denaturants from Multiple Experimental Methods. *J. Am. Chem. Soc.* 138:11714-11726.
42. Schuler B, Lipman EA, & Eaton WA (2002) Probing the free-energy surface for protein folding with single-molecule fluorescence spectroscopy. *Nature* 419:743-747.

43. Hoffmann A*, et al.* (2007) Mapping protein collapse with single-molecule fluorescence and kinetic synchrotron radiation circular dichroism spectroscopy. *Proc. Natl. Acad. Sci. USA* 104:105-110.
44. Case DA*, et al.* (2012) AMBER 12University of California, San Francisco).
45. Doose S, Neuweiler H, & Sauer M (2009) Fluorescence quenching by photoinduced electron transfer: a reporter for conformational dynamics of macromolecules. *Chemphyschem : a European journal of chemical physics and physical chemistry* 10:1389-1398.
46. Khatri BS & McLeish TCB (2007) Rouse model with internal friction: A coarse grained framework for single biopolymer dynamics. *Macromolecules* 40:6770-6777.
47. Hagen SJ, Hofrichter J, Szabo A, & Eaton WA (1996) Diffusion-limited contact formation in unfolded cytochrome c: estimating the maximum rate of protein folding. *Proc. Natl. Acad. Sci. USA* 93:11615-11617.
48. Krieger F, Fierz B, Bieri O, Drewello M, & Kiefhaber T (2003) Dynamics of unfolded polypeptide chains as model for the earliest steps in protein folding. *J. Mol. Biol.* 332:265-274.
49. Neuweiler H, Schulz A, Bohmer M, Enderlein J, & Sauer M (2003) Measurement of submicrosecond intramolecular contact formation in peptides at the single-molecule level. *J. Am. Chem. Soc.* 125:5324-5330.
50. Doose S, Neuweiler H, & Sauer M (2005) A close look at fluorescence quenching of organic dyes by tryptophan. *Chemphyschem : a European journal of chemical physics and physical chemistry* 6:2277-2285.
51. Wunderlich B*, et al.* (2013) Microfluidic mixer designed for performing single-molecule kinetics with confocal detection on timescales from milliseconds to minutes. *Nature Protocols* 8:1459-1474.
52. Neuweiler H, Lollmann M, Doose S, & Sauer M (2007) Dynamics of unfolded polypeptide chains in crowded environment studied by fluorescence correlation spectroscopy. *J. Mol. Biol.* 365:856-869.
53. Buscaglia M, Lapidus LJ, Eaton WA, & Hofrichter J (2006) Effects of denaturants on the dynamics of loop formation in polypeptides. *Biophys. J.* 91:276-288.
54. Makarov DE (2010) Spatiotemporal correlations in denatured proteins: The dependence of fluorescence resonance energy transfer (FRET)-derived protein reconfiguration times on the location of the FRET probes. *J. Chem. Phys.* 132:035104.
55. Szabo A, Schulten K, & Schulten Z (1980) 1st Passage Time Approach to Diffusion Controlled Reactions. *J. Chem. Phys.* 72:4350-4357.
56. Vaiana AC*, et al.* (2003) Fluorescence quenching of dyes by tryptophan: Interactions at atomic detail from combination of experiment and computer simulation. *J. Am. Chem. Soc.* 125:14564-14572.
57. Lapidus LJ, Eaton WA, & Hofrichter J (2001) Dynamics of intramolecular contact formation in polypeptides: Distance dependence of quenching rates in a room-temperature glass - art. no. 258101. *Phys. Rev. Lett.* 8725:8101-+.
58. Toan NM, Morrison G, Hyeon C, & Thirumalai D (2008) Kinetics of loop formation in polymer chains. *J Phys Chem B* 112:6094-6106.
59. Alexander-Katz A, Wada H, & Netz RR (2009) Internal Friction and Nonequilibrium Unfolding of Polymeric Globules. *Phys. Rev. Lett.* 103.
60. Schulz JCF, Miettinen MS, & Netz RR (2015) Unfolding and Folding Internal Friction of beta-Hairpins Is Smaller than That of alpha-Helices. *J. Phys. Chem. B* 119:4565-4574.
61. Gopich IV, Nettels D, Schuler B, & Szabo A (2009) Protein dynamics from single-molecule fluorescence intensity correlation functions. *J. Chem. Phys.* 131.

62. Müller-Späth S*, et al.* (2010) Charge interactions can dominate the dimensions of intrinsically disordered proteins. *Proc. Natl. Acad. Sci. USA* 107:14609-14614.
63. Konig I*, et al.* (2015) Single-molecule spectroscopy of protein conformational dynamics in live eukaryotic cells. *Nat. Methods* 12:773-779.
64. Wuttke R*, et al.* (2014) Temperature-dependent solvation modulates the dimensions of disordered proteins. *Proc. Natl. Acad. Sci. USA* 111:5213-5218.
65. de Gennes PG (1979) *Scaling concepts in polymer physics* (Cornell University Press, Ithaca, N.Y.) p 324 p.
66. Müller BK, Zaychikov E, Bräuchle C, & Lamb DC (2005) Pulsed interleaved excitation. *Biophys. J.* 89:3508-3522.
67. Haenni D, Zosel F, Reymond L, Nettels D, & Schuler B (2013) Intramolecular Distances and Dynamics from the Combined Photon Statistics of Single-Molecule FRET and Photoinduced Electron Transfer. *J. Phys. Chem. B* 117:13015-13028.
68. Nettels D, Hoffmann A, & Schuler B (2008) Unfolded Protein and Peptide Dynamics Investigated with Single-Molecule FRET and Correlation Spectroscopy from Picoseconds to Seconds. *J. Phys. Chem. B* 112:6137-6146.
69. Lakowicz JR (2006) *Principles of fluorescence spectroscopy* (Springer, New York) 3rd Ed pp xxvi, 954 p.
70. Schuler B, Müller-Späth S, Soranno A, & Nettels D (2012) Application of confocal single-molecule FRET to intrinsically disordered proteins. *Methods Mol. Biol.* 896:21-45.
71. Sisamakis E, Valeri A, Kalinin S, Rothwell PJ, & Seidel CAM (2010) Accurate Single-Molecule FRET Studies Using Multiparameter Fluorescence Detection. *Methods Enzymol.* 475:455-514.
72. Aznauryan M*, et al.* (2016) Comprehensive structural and dynamical view of an unfolded protein from the combination of single-molecule FRET, NMR, and SAXS. *Proc Natl Acad Sci U S A* 113:E5389–E5398.
73. Scalley ML & Baker D (1997) Protein folding kinetics exhibit an Arrhenius temperature dependence when corrected for the temperature dependence of protein stability. *Proc. Natl. Acad. Sci. USA* 94:10636-10640.
74. Vitalis A & Pappu RV (2009) Methods for Monte Carlo Simulations of Biomacromolecules. *Annual Reports in Computational Chemistry, Vol 5* 5:49-76.
75. Uzawa T, Cheng RR, Cash KJ, Makarov DE, & Plaxco KW (2009) The Length and Viscosity Dependence of End-to-End Collision Rates in Single-Stranded DNA. *Biophys. J.* 97:205-210.
76. Gopich IV & Szabo A (2006) Theory of the statistics of kinetic transitions with application to single-molecule enzyme catalysis. *J. Chem. Phys.* 124.
77. Kabsch W & Sander C (1983) Dictionary of Protein Secondary Structure - Pattern-Recognition of Hydrogen-Bonded and Geometrical Features. *Biopolymers* 22:2577-2637.